Stitching Dynamic Movement Primitives and Image-Based Visual Servo Control

Ghananeel Rotithor, *Graduate Student Member, IEEE*, Iman Salehi, *Member, IEEE*, Edward Tunstel, *Fellow, IEEE*, and Ashwin P. Dani, *Senior Member, IEEE*

***Abstract*—Utilizing perception for feedback control in combination with dynamic movement primitive (DMP)-based motion generation for a robot's end-effector control is a useful solution for many robotic manufacturing tasks. For instance, while performing an insertion task when the hole or the recipient part is not visible in the eye-in-hand camera, a learning-based movement primitive method can be used to generate the end-effector path. Once the recipient part is in the field of view (FOV), image-based visual servo (IBVS) can be used to control the motion of the robot. Inspired by such applications, this article presents a generalized control scheme that switches between motion generation using DMP and IBVS control. To facilitate the design, a common state-space representation for the DMP and the IBVS systems is first established. The stability analysis of the switched system using multiple Lyapunov functions shows that the state trajectories converge to a bound asymptotically. The developed method is validated by three real-world experiments using the eye-in-hand configuration of a Baxter research robot.**

***Index Terms*—Image-based visual servo (IBVS) control, learning from demonstration, robot control, visual servoing.**

I. Introduction

ROBOTS are required to perform fine manipulation, navigation, and target tracking tasks in a variety of applications ranging from manufacturing automation to space exploration. To perform tasks involving fine manipulation, incorporating visual feedback can be beneficial when the robot end effector is close to the object being manipulated. To perform tasks such as landing a quadcopter from a far away distance, incorporating visual feedback is useful when image features are visible to an onboard camera sensor. When the object is not in the field of view (FOV) of the camera or reliable features cannot be extracted or if there is a feature loss, learning-based motion generation methods, such as dynamic movement primitives (DMPs), can be used to control the robot. For example, in a wire pinning task for wire harness assembly, the robot holding the wire should reach the pin by following a certain trajectory that avoids collision with the fixtures holding the pin. The pin may not always be in the FOV of the camera attached to the robot end effector. In such cases, to insert the wire into the pin, a learned DMP can be used to generate the motion that takes the wire near to the pin before the visual feedback of the pin is available [1]. Motivated by such examples and a need to ensure stable motion when switching between learned and vision-based controllers, a new methodology that unifies DMP [2] and image-based visual servoing (IBVS) [3] is proposed in this article. The proposed algorithm enables stable switching between DMP and IBVS controllers to reach the goal location from an initial location when the visual feedback is not continuously available. The proposed switched system is referred to as a DMP-IBVS switched system.

Many approaches have been developed to design robot controllers using visual feedback that keep the objects in the FOV (see [4], [5], [6]). A trajectory planning and tracking control approach for mobile robots is developed in [7] that uses virtual-goal-guided rapidly exploring random tree (RRT) for trajectory planning and IBVS with the FOV constraints for tracking. A constrained IBVS approach for helicopter landing on a moving platform is proposed in [8] using a control barrier function methodology to satisfy the FOV constraints. A model predictive controller (MPC) for visual servoing of a mobile robot is developed in [9] which handles visibility constraints for IBVS and velocity limits of the robot. In contrast, a learning-based robot motion generation using DMP is developed in this article to generate robot control commands in the absence of visual feedback, and a switching control law is developed to switch to the IBVS controller when visual feedback is available.

It is known that switching arbitrarily between stable subsystems can lead to instability [10], [11]. In [12], an average dwell-time condition based on multiple Lyapunov functions is developed for stabilizing switched systems. Daafouz et al. [13] proposed a linear matrix inequality-based condition to check for the existence of a quadratic Lyapunov function for proving the asymptotic stability of a switched discrete system. In [14], LaSalle's invariance principle is extended to switched linear systems to deduce asymptotic stability using multiple Lyapunov functions whose Lie derivatives are negative semidefinite. In [15], a survey of results for the stability of

Manuscript received 23 February 2022; accepted 28 September 2022. This work was supported in part by the Space Technology Research Institutes through the NASA Space Technology Research Grants Program under Grant 80NSSC19K1076, and in part by NSF under Grant SMA-2134367. This article was recommended by Associate Editor G. Pandey. *(Corresponding author: Ashwin P. Dani.)*

Ghananeel Rotithor, Iman Salehi, and Ashwin P. Dani are with the Department of Electrical and Computer Engineering, University of Connecticut, Storrs, CT 06269 USA (e-mail: ghananeel.rotithor@uconn.edu; iman.salehi@uconn.edu; ashwin.dani@uconn.edu).

Edward Tunstel was with the Department of Autonomous and Intelligent Systems, Raytheon Technologies Research Center, East Hartford, CT 06108 USA. He is now with Motiv Space Systems Inc., Pasadena, CA 91107 USA (e-mail: tunstel@ieee.org).

This article has supplementary material provided by the authors and color versions of one or more figures available at https://doi.org/10.1109/TSMC.2022.3214756.

Digital Object Identifier 10.1109/TSMC.2022.3214756

switched linear systems is presented, and the problem of stabilizability of switched systems is analyzed. Multiple Lyapunov functions for analyzing Lyapunov stability and iterated function systems as a tool for Lagrange stability are proposed in [16]. Invariance-like results for nonautonomous nonlinear switched systems are developed in [17]. Switched systems analysis of output-feedback systems and observers have been studied in the literature. The switching method in [18] analyzes switching between locally and globally converging observers with asymptotic stability. A composite output-feedback control law is derived in [19] that switches between locally and globally asymptotically stable output-feedback controllers.

Switched systems analysis has been used to solve challenging problems in robotics, including visual servo control and vision-based trajectory tracking. In [20], an asymptotically stable hybrid switched systems visual servo controller is proposed, which switches between IBVS and position-based visual servo control (PBVS) based on multiple Lyapunov functions. The switching between IBVS-PBVS control is developed to switch between unstable systems and increase the region of stability. An estimator that switches between the state predictor and the image-based observer for object localization is presented in [21] when the image feedback is intermittently available. The stability of the switched system is established using a common Lyapunov function. An estimator for pose estimation of a moving target is developed in [22] when measurements are available intermittently by learning the motion model. In [23] and [24], an observer–predictor framework is presented for target tracking and trajectory tracking in the presence of intermittent measurements by switching between a global uniformly ultimately bounded (GUUB) and an unstable system. The switched error system is shown to be GUUB based on the dwell-time conditions. The approaches for image-based tracking use switching between systems mainly to accommodate feature track losses, occlusions, and limited camera FOV of features. Switched systems analysis is also developed for target tracking in the presence of intermittent observations from a network of stationary cameras in [25]. In [26], consensus protocols of a distributed multiagent system are developed using switched systems analysis wherein the leader provides intermittent information to all the followers. The application of the switched system to biped locomotion is developed in [27] where the boundedness of input-to-state (ISS) stable switched systems with multiple equilibria is proven. The switched system results developed or applied in these results switch between systems that are either globally stable or locally stable.

In contrast to the switched systems approaches developed to handle feature track losses, occlusions in object tracking and localization, and approaches developed to improve the stability in IBVS-PBVS switching, this article develops a new method that switches between image-based control and learning-based control when the image feedback is not available such as in instances which may include limited camera FOV, occlusions, and feature losses. In this article, a new switched systems analysis is developed for systems that switch between locally stable (IBVS system) and globally stable (DMP system) modes. The goal is to regulate the camera pose with respect to a target. When visual feedback is available, the IBVS controller is used to generate camera accelerations. When visual feedback is not available, then DMP is used to generate camera accelerations. DMP is implemented as an online end-effector acceleration controller whose weights are trained using a pose regulation task demonstration data. The method can be useful in robotic tasks where a robot arm with eye-in-hand configuration is controlled using DMP and IBVS controllers for achieving precision or when a ground robot is controlled using a camera mounted on the robot with image and nonimage feedback. The technical contributions of this article are as follows.

1) A new common state-space representation is developed to analyze the switched system stability of the IBVS and DMP acceleration controllers.
2) A new IBVS acceleration control law is developed and the corresponding closed-loop dynamics are proven to be uniformly ultimately bounded (UUB) if the initial state is sufficiently close to the goal state.
3) Combined position and orientation DMPs are presented and the corresponding dynamics are proven to be globally asymptotically stable.
4) The switching between the locally stable IBVS controller and globally stable DMP is analyzed using multiple Lyapunov functions and the switched system dynamics are proven to converge asymptotically to a bound whose analytical expression is derived. Furthermore, an algorithm is developed based on the analysis of the switched system to ensure stable switching between the IBVS and DMP subsystems.

Compared to our preliminary development in [28], this article provides rigorous stability analyses for the individual DMP and IBVS systems along with a method for switching and stability analysis for the switched system. Experimental results for a pose regulation task are presented using the eye-in-hand configuration of the Baxter robot, and the switched system results are validated in the presence of occlusions in the image feedback and compared with a DMP-only controller.

The remainder of this article is organized as follows. In Section II, the coordinate frames attached to the robot base, camera, the goal location, and its kinematics are discussed. In Section III, an acceleration controller is presented for IBVS and the error dynamics are proven to be UUB. In Section IV, position and orientation DMPs are presented and global asymptotic stability of the error dynamics is presented. In Section V, the stability of the switched system is proven and an average dwell-time condition is developed. Experimental results of the switched system are presented in Section VI.

Notations: The set of real numbers and integers is denoted by $\mathbb{R}$ and $\mathbb{Z}$, respectively. The symbols $\mathbb{R}^+$ and $\mathbb{Z}^+$ denote the set of non-negative real numbers and non-negative integers, respectively. The standard Euclidean norm of a vector is denoted by $\|\cdot\|$ and for a p-dimensional real vector, the open ball is defined as $\mathcal{B}_\zeta(x) = \{x' \in \mathbb{R}^p \mid \|x - x'\| < \zeta\}$, where $\zeta > 0$ is a constant. For a matrix $A \in \mathbb{R}^{n\times n}$, its symmetric part is denoted by $\text{sym}\{A\} = (1/2)(A + A^T)$.

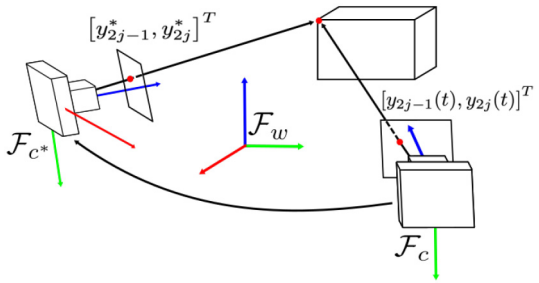

Fig. 1. Reference frames attached to the camera, the goal location, and the inertial reference frame.

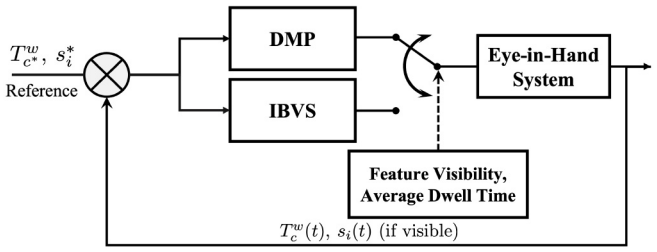

Fig. 2. Block diagram of the DMP-IBVS switched system.

II. Problem Formulation

Consider a fixed inertial reference frame $\mathcal{F}_w$ attached to the robot base and a coordinate frame $\mathcal{F}_c$ attached to a moving camera observing a static object shown in Fig. 1. The camera frame $\mathcal{F}_c$ is attached to the camera in such a way that the z-axis of the coordinate frame aligns with the optical axis of the camera and the x- and y-axes form the basis of the image plane. Thus, the coordinate frame attached to the camera always moves along with it, as the camera undergoes motion. Let $R^a_b \in SO(3)$ and $t^a_b \in \mathbb{R}^3$ be the rotation and translation from a to b expressed in a, respectively. A quaternion representation of the rotation matrix R^a_b is given by $q^a_b \in \mathcal{S}^4$, where $\mathcal{S}^p = \{x \in \mathbb{R}^p | x^T x = 1\}$ is the unit hypersphere. It is assumed that the pose of the camera in the world reference frame $T^w_c(t)$ can be measured. A coordinate frame $\mathcal{F}_{c^*}$ is attached to the desired goal location such that when $\mathcal{F}_c$ coincides with $\mathcal{F}_{c^*}$ the image feature error and the pose error are zero. Additionally, the pose transformation between $\mathcal{F}_w$ and $\mathcal{F}_{c^*}$, denoted as $T^w_{c^*}$, is assumed to be known. The time-varying pose transformation between the goal camera frame and the current camera frame is denoted by $T^{c^*}_c(t)$ and is represented as $[(t^{c^*}_c(t))^T, (q^{c^*}_c(t))^T]^T \in \mathbb{R}^3 \times \mathcal{S}^4$.

For designing a switching control law between DMP and IBVS, a common state space is established between them. A new common auxiliary state is defined as follows:

$$x(t) = \begin{bmatrix} e_p^T(t) & \xi^T_{c^*}(t) \end{bmatrix}^T \in \mathbb{R}^{12} \tag{1}$$

where $e_p(t) = [(t^{c^*}_c(t))^T, r^T(t)]^T \in \mathbb{R}^6$ and $r(t) = 2\log(q^{c^*}_c(t)) = \Theta(t)\mathbf{n}(t)$ is the quaternion logarithm that transforms a quaternion into the corresponding angle–axis product where $-\pi < \Theta(t) < \pi$. The pose transformation $e_p(t)$ can be viewed as the pose error that indicates the deviation of the current camera frame $\mathcal{F}_c$ from the goal camera frame $\mathcal{F}_{c^*}$. In (1), $\xi_{c^*}(t) = [\, v^T_{c^*}(t)\ \omega^T_{c^*}(t)\,]^T \in \mathbb{R}^6$ is the velocity of the camera expressed in the desired frame $\mathcal{F}_{c^*}$, such that $v_{c^*}(t) \in \mathbb{R}^3$ is the linear velocity and $\omega_{c^*}(t) \in \mathbb{R}^3$ is the angular velocity.

Problem Description and Solution Approach: Given the desired pose $T^w_{c^*}$, and the current camera pose $T^w_c(t)$, the problem is to regulate the current camera frame $\mathcal{F}_c$ to the goal camera frame $\mathcal{F}_{c^*}$ using both the image feedback when it is available and a learned DMP when image feedback is not available. A stable switching controller is developed, which switches between the DMP and the IBVS control. The switching is triggered when the image features are visible in the camera FOV. The feature points may or may not be visible depending on the current camera pose. In such cases, the camera motion control is switched to DMP. A block diagram of the DMP and IBVS switching mechanism is shown in Fig. 2.

In the following sections, the details of the IBVS controller and the DMP are first presented, followed by a stability analysis of the switched controller.

III. Image-Based Visual Servo Control

The objective of IBVS is to regulate image plane feature errors to zero. Let the state vector for the current image plane features be denoted by $s_i(t) = [\, y_1(t), \cdots y_{2m}(t)\,]^T \in \mathbb{R}^{2m}$ and let the goal feature vector be denoted by $s^*_i = [\, y^*_1, \cdots y^*_{2m}\,]^T$, where m is the number of feature points. Each feature is represented by its X and Y locations in the image plane. The dynamics of the features $s_i(t)$ can be expressed as

$$\dot{s}_i(t) = L_i(s_i(t), Z(t))\xi_c(t) \tag{2}$$

where $L_i(s_i, Z) \in \mathbb{R}^{2m\times 6}$ is the interaction matrix and $Z(t) = [\, Z_1(t) \cdots Z_m(t)\,]^T \in \mathbb{R}^m$ is the time-varying depth of the feature points with respect to the camera frame. In (2), the vector $\xi_c(t) = [\, v^T_c(t)\ \omega^T_c(t)\,]^T$ contains the linear and angular camera velocities expressed in the camera frame $\mathcal{F}_c$ in twist coordinates. The dependence of the variables on time and other arguments is dropped in the rest of this article unless stated. In (2), the interaction matrix is given by $L_i(s_i, Z) = [\, L^T_{i_1}(y_1, y_2, Z_1) \cdots L^T_{i_m}(y_{2m-1}, y_{2m}, Z_m)\,]^T$, where

$$L_{i_j} = \begin{bmatrix} \frac{-1}{Z_j} & 0 & \frac{y_{2j-1}}{Z_j} & y_{2j-1}y_{2j} & -\left(1+y^2_{2j-1}\right) & y_{2j} \\ 0 & \frac{-1}{Z_j} & \frac{y_{2j}}{Z_j} & 1+y^2_{2j} & -y_{2j-1}y_{2j} & -y_{2j-1} \end{bmatrix}$$
$$\forall j = 1, \ldots, m. \tag{3}$$

The corresponding error vector between the current and the goal image features is defined as $e_i(t) = s_i(t) - s^*_i$. The error dynamics are given by

$$\dot{e}_i = L_i(s_i, Z)\xi_c. \tag{4}$$

Taking the time derivative of (4) yields the following second-order dynamics:

$$\ddot{e}_i = L_i(s_i, Z)\dot{\xi}_c + \dot{L}_i\big(s_i, \dot{s}_i, Z, \dot{Z}\big)\xi_c. \tag{5}$$

Motivated by the stability analysis, the following acceleration control law is designed:

$$\dot{\xi}_c = \widehat{L}^+_i\big(s_i, Z^\star\big)\Big(-k_p e_i - k_v \dot{\hat{e}}_i\Big) \tag{6}$$

where $k_p, k_v > 0$ are the controller gains, and $\dot{\hat{e}}_i$ is an approximation of $\dot{e}_i(t)$, which either can be computed numerically or using an approximation of $Z(t)$ in (4). In this article, the depth is approximated by the constant desired depth $Z^\star$ to construct $\widehat{L}_i$.

Assumption 1: The approximation error $\chi(t) = \dot{e}(t) - \dot{\hat{e}}_i(t)$ is bounded by a constant, i.e., $\exists \bar{\chi} \in [0, \infty)$ such that $\sup_{t\geq 0} \|\chi(t)\| \leq \bar{\chi}$.

Remark 1: The validity of Assumption 1 can be ensured using a suitable numerical approximation to compute $\dot{\hat{e}}_i$. For example, the finite difference method with smoothing or polynomial regression method over a time window can be used.

In (6), $\widehat{L}_i^+ = (\widehat{L}_i^T \widehat{L}_i)^{-1} \widehat{L}_i^T$ is the pseudoinverse of $\widehat{L}_i$. Using the relation $\dot{\hat{e}}_i(t) = \dot{e}_i(t) - \chi(t)$, and (4)–(6), the resulting closed-loop second-order dynamics can be written as

$$\ddot{e}_i = -k_p L_i \widehat{L}_i^+ e_i - k_v L_i \widehat{L}_i^+ \dot{e}_i + \dot{L}_i \xi_c + k_v L_i \widehat{L}_i^+ \chi. \tag{7}$$

To facilitate the stability analysis of the switched controller, the dynamics of the state defined in (1) are first established. To this end, a locally injective nonlinear function $\phi : \mathbb{R}^6 \to \mathbb{R}^{2m}$ which maps the pose error $e_p(t)$ to the image error $e_i(t)$ as $e_i(t) = \phi(e_p(t))$ is used as described in [20], where $\phi(0) = 0$. Let $\rho(t) = [\, e_i^T(t) \; \dot{e}_i^T(t) \,]^T \in \mathbb{R}^{4m}$. The following relation is obtained using the result in (4):

$$\rho = \begin{bmatrix} \phi(e_p) \\ L_i \mathbf{R} \xi_{c^*} \end{bmatrix}, \mathbf{R} = \begin{bmatrix} R_{c^*}^c & 0_{3\times 3} \\ 0_{3\times 3} & R_{c^*}^c \end{bmatrix}. \tag{8}$$

From (8), $\rho(t) = 0$ when $x(t) = [e_p^T(t), \xi_{c^*}^T(t)]^T = 0$. Using the mean value theorem and the development in [29, Ch. 4] for (8) at $x(t) = 0$ yields

$$\begin{aligned} \rho &= \begin{bmatrix} J_1 & 0_{2m\times 6} \\ 0_{2m\times 6} & J_2 \end{bmatrix} \begin{bmatrix} e_p \\ \xi_{c^*} \end{bmatrix} + \mathcal{O}(x) \\ \rho &= \mathbf{J} x + \mathcal{O}(x) \end{aligned} \tag{9}$$

where $\mathbf{J} \in \mathbb{R}^{4m\times 12}$ is the Jacobian, $J_1 = (\partial\phi/\partial e_p)|_{e_p=0}$, $J_2 = L_i(s_i^*, Z^\star)\mathbf{R}$, the term $\mathcal{O}(x)$ satisfies $\mathcal{O}(x) \leq \upsilon_1 \|x\|$, where $\upsilon_1 \in \mathbb{R}^+$. The Jacobian $\mathbf{J}$ is full-column rank in the neighborhood of $x(t) = 0$ as $\phi(\cdot)$ is locally injective and J_2 can be made full-column rank by selecting an appropriate desired feature vector s_i^*.

To facilitate the stability analysis of the switched system, using the dynamics of $\dot{e}_p(t)$ derived in [20, Sec. II-B], the dynamics of the common state $x(t)$ for IBVS can be concisely written as a first-order dynamical system of the form

$$\dot{x} = f_v(x, t) + g_v(t) \tag{10}$$

where $f_v : \mathbb{R}^{12} \times \mathbb{R}^+ \to \mathbb{R}^{12}$ is a locally Lipschitz function, whose form can be derived using the injective function ϕ, (8), and (4) and $g_v(t) = [\, 0_{1\times 6}^T \; (k_v \mathbf{R}^T \widehat{L}_i^+ \chi(t))^T \,]^T$ is a perturbation term. To facilitate the stability analysis of the system in (10), the following remarks and assumptions are stated.

Remark 2: Using the relation in (4), the upper bound on the norm of the velocity is given by $\|\xi_c\| \leq (\inf_{t\geq 0} \sigma_{\min}(L_i))^{-1} \|\dot{e}_i\|$, where $\sigma_{\min}(L_i)$ is the minimum nonzero singular value of the matrix $L_i(s_i, Z)$.

Assumption 2: The matrices $\widehat{L}_i^+(s_i, Z^\star)$ and $\dot{L}_i(s_i, \dot{s}_i, Z, \dot{Z})$ can be upper bounded using the constants $l_1, l_2 > 0$ as $\sup_{t\geq 0,\, \|\dot{e}_1\|=1} \|\widehat{L}_i^+\| \leq l_1$ and $\sup_{t\geq 0,\, \|\dot{e}_i\|=1} \|\dot{L}_i\| \leq l_2$ in a sufficiently small neighborhood of the origin.

Remark 3: Assumption 2 is mild since it only requires $s_i(t)$, $Z(t)$ to be bounded in a local region near s_i^* [30, Remark 1]. The bound on the matrix $\dot{L}_i(s_i, \dot{s}_i, Z, \dot{Z})$ holds given that $s_i(t)$, $Z(t)$ are bounded, since $\dot{Z}(t)$ is a function of the bounded 3-D coordinates of the feature point and the velocity vector $\xi_c(t)$ ([31, Ch. 12, p. 414]), which can be upper bounded using Remark 2.

Assumption 3: The matrix $\widehat{L}_i^+$ is constructed using suitable feature points and a constant depth approximation such that in a sufficiently small neighborhood of the origin, $e_i(t), \dot{e}_i(t) \notin \mathrm{Ker}\{\widehat{L}_i^+\}$, $\widehat{L}_i^+ L_i > 0$ and $\widehat{L}_i^+$ has full-column rank as described in [32].

Remark 4: Assumption 3 implies that if the matrix $\widehat{L}_i^+$ is suitably computed and the initial camera pose is in a local neighborhood of the goal camera pose, then the feature motion is realizable which ensures the final camera pose does not reach a local minimum. In this local region, the matrix $\widehat{L}_i^+ L_i$ is positive definite [3], [32].

Theorem 1: If Assumptions 1–3 hold, then the dynamics in (10) are UUB in the sense that for an initial time $t_0 \geq 0$ if

$$\|x_0\| < \sqrt{\frac{\underline{\gamma_v}}{\overline{\gamma_v}}} \delta_1 \Rightarrow \limsup_{t\to\infty} \|x(t)\| \leq \sqrt{\frac{\overline{\gamma_v}}{\underline{\gamma_v}} \frac{\eta}{\beta_1}} \tag{11}$$

where $x_0 = x(t_0)$, provided that $\delta_1 > \sqrt{\overline{\gamma_v}\eta/\underline{\gamma_v}\beta_1}$, and the controller gains k_p and k_v satisfy the sufficient condition

$$\lambda_v = \lambda_{\min} \begin{bmatrix} \frac{\varepsilon_1 k_p \underline{k}}{2} & k^\star \\ k^\star & k_v \underline{k} - \frac{\varepsilon_1 \bar{l}}{2} \end{bmatrix} > 0 \tag{12}$$

where $k^\star = -(\bar{l}/2) - (\bar{k}/2)(k_p + [\varepsilon_1 k_v/2])$ and ε_1, $\underline{k}$, $\bar{l}$, $\bar{k}$, $\overline{\gamma_v}$, $\underline{\gamma_v}$, β_1, η, δ_1 are positive constants.

Proof: Using (9), the following upper and lower bounds $\underline{m}\|x\|^2 \leq \|\rho\|^2 \leq \bar{m}\|x\|^2$ can be derived where $\underline{m} = \lambda_{\min}(\mathbf{J}^T\mathbf{J})$ and $\bar{m} = \lambda_{\max}(\mathbf{J}^T\mathbf{J}) + \bar{\upsilon}_1$, where $\bar{\upsilon}_1 \in \mathbb{R}^+$. The operators $\lambda_{\min}(\cdot)$ and $\lambda_{\max}(\cdot)$ correspond to the minimum nonzero and maximum eigenvalues of the matrix. Consider a candidate Lyapunov function $V_v(x, t) : \mathcal{B}_{\delta_1}(0) \times \mathbb{R}^+ \to \mathbb{R}^+$ such that $\mathcal{B}_{\delta_1}(0) \subset \mathbb{R}^{12}$ and

$$V_v(x, t) = x^T P_v(t) x + \tilde{\mathcal{O}}(x) = \rho^T Q(t) \rho \tag{13}$$

with $\tilde{\mathcal{O}}(x) \leq \upsilon_2 \|x\|^2$ indicating the remaining terms, where $\upsilon_2 \in \mathbb{R}^+$. In (13), $P_v(t) = \mathbf{J}^T Q(t) \mathbf{J}$ and Q is expressed as

$$Q = \begin{bmatrix} \frac{1}{2}(\widehat{L}_i^+)^T \widehat{L}_i^+ & \frac{\varepsilon_1}{4}(\widehat{L}_i^+)^T \widehat{L}_i^+ \\ \frac{\varepsilon_1}{4}(\widehat{L}_i^+)^T \widehat{L}_i^+ & \frac{1}{2}(\widehat{L}_i^+)^T \widehat{L}_i^+ \end{bmatrix} \tag{14}$$

where $\varepsilon_1 > 0$ is a suitably chosen constant. Although $Q(t)$ is positive semidefinite, it is known from Assumption 3 that $e_i(t), \dot{e}_i(t) \notin \mathrm{Ker}\{\widehat{L}_i^+\}$ if the initial pose of the camera is close to the goal pose, which is enough to ensure that the quadratic form in (13) is always nonzero in a local region near the origin and is zero at the origin. The Lyapunov function in (13) can be then upper and lower bounded as $\underline{\gamma_v}\|x\|^2 \leq V_v(x, t) \leq \overline{\gamma_v}\|x\|^2$, where $\underline{\gamma_v} = \inf_{t\geq 0} \lambda_{\min}(P_v)$ and $\overline{\gamma_v} = \sup_{t\geq 0} \lambda_{\max}(P_v) + \upsilon_2$.

Taking the time derivative of (13), using (4) and (7), $\dot{V}_v$ can be written as

$$\begin{aligned}\dot{V}_v = {} & e_i^T\big(\widehat{L}_i^+\big)^T\widehat{L}_i^+\dot{e}_i + \dot{e}_i^T\big(\widehat{L}_i^+\big)^T\widehat{L}_i^+\dot{L}_i\xi_c \\ & - k_p\dot{e}_i^T\big(\widehat{L}_i^+\big)^T\widehat{L}_i^+L_i\widehat{L}_i^+e_i - k_v\dot{e}_i^T\big(\widehat{L}_i^+\big)^T\widehat{L}_i^+L_i\widehat{L}_i^+\dot{e}_i \\ & + k_v\dot{e}_i^T\big(\widehat{L}_i^+\big)^T\widehat{L}_i^+L_i\widehat{L}_i^+\chi \;\; + \frac{\varepsilon_1}{2}\dot{e}_i^T\big(\widehat{L}_i^+\big)^T\widehat{L}_i^+\dot{e}_i \\ & + \frac{\varepsilon_1}{2}e_i^T\big(\widehat{L}_i^+\big)^T\widehat{L}_i^+\dot{L}_i\xi_c - \frac{\varepsilon_1 k_p}{2}e_i^T\big(\widehat{L}_i^+\big)^T\widehat{L}_i^+L_i\widehat{L}_i^+e_i \\ & - \frac{\varepsilon_1 k_v}{2}e_i^T\big(\widehat{L}_i^+\big)^T\widehat{L}_i^+L_i\widehat{L}_i^+\dot{e}_i \\ & + \frac{\varepsilon_1 k_v}{2}e_i^T\big(\widehat{L}_i^+\big)^T\widehat{L}_i^+L_i\widehat{L}_i^+\chi \\ & + e_i^T\big(\widehat{L}_i^+\big)^T\dot{\widehat{L}}_i^+e_i + \dot{e}_i^T\big(\widehat{L}_i^+\big)^T\dot{\widehat{L}}_i^+\dot{e}_i \\ & + \frac{\varepsilon_1}{2}e_i^T\big(\widehat{L}_i^+\big)^T\dot{\widehat{L}}_i^+\dot{e}_i + \frac{\varepsilon_1}{2}e_i^T\Big(\dot{\widehat{L}}_i^+\Big)^T\widehat{L}_i^+\dot{e}_i. \end{aligned} \tag{15}$$

Using Assumption 3, it can be ensured that $\underline{k}\|e_i\|^2 \leq e_i^T\mathrm{sym}\{(\widehat{L}_i^+)^T\widehat{L}_i^+L_i\widehat{L}_i^+\}e_i \leq \bar{k}\|e_i\|^2$ and $\underline{k}\|\dot{e}_i\|^2 \leq \dot{e}_i^T\mathrm{sym}\{(\widehat{L}_i^+)^T\widehat{L}_i^+L_i\widehat{L}_i^+\}\dot{e}_i \leq \bar{k}\|\dot{e}_i\|^2$ for some $\bar{k} \geq \underline{k} > 0$ in the local region near the origin. Using Assumption 2 and defining the following upper bounds in the considered local region as $\sup_{t\geq 0}\|(\widehat{L}_i^+)^T\widehat{L}_i^+\| \leq \bar{l}$, $(\inf_{t\geq 0}\sigma_{\min}\{L_i\})^{-1}\sup_{t\geq 0}\|(\widehat{L}_i^+)^T\widehat{L}_i^+\dot{L}_i\| \;\|\dot{e}_i\| \leq \vartheta\|\dot{e}_i\|^2$, $\sup_{t\geq 0}\|(\widehat{L}_i^+)^T\dot{\widehat{L}}_i^+\| \leq \iota\|\dot{e}_i\|$, $\bar{\varepsilon} = \max\{1, \varepsilon_1/2\}$ such that $\bar{l}$, ϑ, $\iota > 0$. Given that the gains k_p and k_v are chosen according to the sufficient condition in (12), then (15) can be upper bounded as

$$\begin{aligned}\dot{V}_v \leq {} & -\lambda_v\|e_i\|^2 - \lambda_v\|\dot{e}_i\|^2 + \bar{\varepsilon}\bar{k}k_v\bar{\chi}(\|e_i\| + \|\dot{e}_i\|) \\ & + \iota\|e_i\|^2\|\dot{e}_i\| + \frac{\varepsilon_1}{2}(\vartheta + 2\iota)\|e_i\|\|\dot{e}_i\|^2 + (\iota + \vartheta)\|\dot{e}_i\|^3. \end{aligned} \tag{16}$$

Using the inequality $\|e_i\| + \|\dot{e}_i\| \leq \sqrt{2(\|e_i\|^2 + \|\dot{e}_i\|^2)} = \sqrt{2}\|\rho\|$, after some algebraic manipulations and using the bounds on $\|\rho\|$ and $\|x\|$, (16) can be simplified to

$$\dot{V}_v \leq -\frac{\beta_1}{\overline{\gamma}_v}V_v + \eta \tag{17}$$

$\forall\|\rho\| \leq (\lambda_v/[2\sqrt{2}\max\{(\varepsilon_1/2)(\vartheta + 2\iota), (\iota + \vartheta)\}])$, where $\beta_1 = (\lambda_v\underline{m}/4)$ and $\eta = ([2\overline{m}(\bar{\varepsilon}\bar{k}k_v\bar{\chi})^2]/[\lambda_v\underline{m}])$. The solution to the differential inequality in (17) can be obtained using [29, Lemma 3.4] and is given by

$$V_v(x,t) \leq V_v(x_0,t_0)e^{-\frac{\beta_1}{\overline{\gamma}_v}(t-t_0)} + \frac{\overline{\gamma}_v\eta}{\beta_1}\left(1 - e^{-\frac{\beta_1}{\overline{\gamma}_v}(t-t_0)}\right). \tag{18}$$

From (18) and using the bounds on the Lyapunov function, it can be concluded that $x(t) \in \mathcal{L}_\infty$. Using [29, Th. 4.18], the state is UUB for sufficiently small $\delta_1 > 0$ representing the local region of convergence, where the relation in (9), Assumptions 2 and 3, and (17) holds. ■

The ultimate bound on the state can be made arbitrarily small by adjusting the controller gains k_p and k_v and by choosing an appropriate approximation method for $\dot{\hat{e}}_i(t)$, which minimizes $\bar{\chi}$.

IV. Task Space Dynamic Movement Primitives

This section describes the position and orientation DMPs which can generate goal reaching motions while retaining the desired shape of the trajectory.

A. Combined Position and Orientation DMPs

To regulate the position and orientation error to zero, i.e., $\|e_p(t)\| \to 0$ and to retain the desired shape of the trajectory, the combined position and orientation DMPs are described by the following acceleration law:

$$\tau^2\dot{\xi}_{c^*} = -\Gamma e_p - \tau\Lambda\xi_{c^*} + \Theta^T\Psi(z_p, z_o) \tag{19}$$

where $\xi_{c^*}(t)$ is the velocity of the camera in the frame $\mathcal{F}_{c^*}$, $\Gamma = \mathrm{diag}\{(\alpha_v\beta_v)\mathrm{I}_3, (\alpha_\omega\beta_\omega)\mathrm{I}_3\}$, $\Lambda = \mathrm{diag}\{\alpha_v\mathrm{I}_3, \alpha_\omega\mathrm{I}_3\}$ such that $\alpha_v, \alpha_\omega, \beta_v, \beta_\omega > 0$ are constant positive gains and $\tau > 0$ is the temporal scaling constant. The third term on the RHS of (19) is a nonlinear forcing function which encodes the shape of the desired trajectory, Θ and Ψ are defined as

$$\Theta = \begin{bmatrix}\theta_p & 0_{N_p\times 3}\\ 0_{N_o\times 3} & \theta_o\end{bmatrix},\; \Psi = \begin{bmatrix}\Psi_p(z_p)z_p\\ \Psi_o(z_o)z_o\end{bmatrix} \tag{20}$$

such that $\theta_p \in \mathbb{R}^{N_p\times 3}$ and $\theta_o \in \mathbb{R}^{N_o\times 3}$ are constant weight matrices associated with the vectors of radial basis functions

$$\Psi_p(z_p) = \left[\frac{\psi_1(z_p)}{\sum_{i=1}^{N_p}\psi_i(z_p)}, \ldots, \frac{\psi_{N_p}(z_p)}{\sum_{i=1}^{N_p}\psi_i(z_p)}\right]^T \in \mathbb{R}^{N_p}$$

and

$$\Psi_o(z_o) = \left[\frac{\varphi_1(z_o)}{\sum_{i=1}^{N_o}\varphi_i(z_o)}, \ldots, \frac{\varphi_{N_o}(z_o)}{\sum_{i=1}^{N_o}\varphi_i(z_o)}\right]^T \in \mathbb{R}^{N_o}$$

with $N_p, N_o > 0$ as respective basis numbers. The individual basis functions are defined as $\psi_i(z_p) = \exp(-h_i^\psi(z_p(t) - c_i)^2)$ and $\varphi_i(z_o) = \exp(-h_i^\varphi(z_o(t) - \nu_i)^2)$. The parameters $c_i, \nu_i > 0$ are centers of the basis functions and $h_i^\psi, h_i^\varphi > 0$ are the variances, respectively. In (20), $z_p(t) \in \mathbb{R}$ and $z_o(t) \in \mathbb{R}$ are solutions to first-order scalar differential equations given by

$$\tau\dot{z}_p = -\alpha_{z_p}z_p, \qquad \tau\dot{z}_o = -\alpha_{z_o}z_o \tag{21}$$

where $\alpha_{z_p}, \alpha_{z_o} > 0$ are constant positive gains. To facilitate the stability analysis, the initial conditions for the differential equation in (21) are set to $z_p(t_0), z_o(t_0) = 1$.

Assumption 4: The nonlinear forcing term can be upper bounded as $\|\Theta^T\Psi\| \leq \bar{\Theta}\bar{\Psi}e^{-\underline{\alpha}(t-t_0)}$, where $\underline{\alpha} = (1/\tau)\min\{\alpha_{z_p}, \alpha_{z_o}\}$ when the DMP is active between $[t_0, t)$.

Remark 5: The implication of Assumption 4 is that the matrix Θ is bounded by a constant, i.e., $\sqrt{\lambda_{\max}(\Theta^T\Theta)} \leq \bar{\Theta}$. This holds true since the analytical solution of the optimization problem in (23) depends on the pseudoinverse of the column-wise augmented Ψ matrices and the demonstration trajectories which are bounded.

Thus, based on (1), the dynamics of $\dot{e}_p(t)$ derived in [20, Sec. II-B], and (19), the state dynamics for DMP can be concisely written as

$$\dot{x} = f_d(x,t) + g_d(t) \tag{22}$$

where $f_d : \mathbb{R}^{12}\times\mathbb{R}^+ \to \mathbb{R}^{12}$ is a locally Lipschitz function and $g_d(t) = [\,0_{1\times 6}^T\;(\Theta^T\Psi(z_p, z_o))^T\,]^T$ is a perturbation term.

B. Learning DMP Parameters

Given a demonstration trajectory with $\mathcal{N}$ data points $\{e_p(t_k), \xi_{c^*}(t_k), \dot{\xi}_{c^*}(t_k)\}_{k=0}^{\mathcal{N}-1}$ sampled at the time instants $\{t_k\}_{k=0}^{\mathcal{N}-1}$, the DMP weights are computed by solving the following optimization problem:

$$\Theta^\star = \arg\min_{\Theta} \sum_{k=0}^{\mathcal{N}-1} \Big\| \tau^2 \dot{\xi}_{c^*}(t_k) + \Gamma e_p(t_k) + \tau \Lambda \xi_{c^*}(t_k) - \Theta^T \Psi\big(z_p(t_k), z_o(t_k)\big) \Big\|^2 \tag{23}$$

for suitably chosen values of τ, Γ, and Λ. The centers and variances are calculated as $c_i = e^{-\alpha_{zp}(i-1/N_p-1)}$, $h_i^\psi = (1/[(c_{i+1}-c_i)^2])$, $h_{N_p}^\psi = h_{N_p-1}^\psi$ $\forall i = 1, \ldots, N_p - 1$ and $v_j = e^{-\alpha_{zo}(j-1/N_o-1)}$, $h_j^\varphi = (1/[(v_{j+1}-v_j)^2])$, $h_{N_o}^\varphi = h_{N_o-1}^\varphi$ $\forall j = 1, \ldots, N_o - 1$.

C. Stability Analysis of DMPs

This section presents the stability analysis of the DMP described in Section IV-A.

Property 1 [33]: Based on the definition of $r(t)$ defined after (1), the following relations hold:

$$r^T \dot{r} = r^T \omega_{c^*}, \quad \dot{r}^T \omega_{c^*} = \omega_{c^*}^T \omega_{c^*}. \tag{24}$$

Theorem 2: Provided that Assumption 4 holds, then the system in (22) is globally asymptotically stable in the sense that

$$\lim_{t\to\infty} \|x(t)\| = 0 \tag{25}$$

given that the gains α_v, β_v, α_ω, and β_ω are chosen according to the sufficient condition

$$\alpha_v = 4\beta_v, \ \alpha_\omega = 4\beta_\omega, \ \beta_v > \frac{3\varepsilon_2}{8\tau}, \ \beta_\omega > \frac{3\varepsilon_2}{8\tau} \tag{26}$$

where $\varepsilon_2 \in (0, \sqrt{4\tau^2 \lambda_{\min}(\Gamma)})$ is a positive constant.

Proof: Consider the candidate Lyapunov function $V_d(x) : \mathbb{R}^{12} \to \mathbb{R}^+$ defined as

$$V_d(x) = x^T P_d x \tag{27}$$

where

$$P_d = \begin{bmatrix} \frac{1}{2}\Gamma & \frac{\varepsilon_2}{4} I_6 \\ \frac{\varepsilon_2}{4} I_6 & \frac{\tau^2}{2} I_6 \end{bmatrix}.$$

The Lyapunov function in (27) is upper and lower bounded as $\underline{\gamma_d}\|x\|^2 \le V_d(x) \le \overline{\gamma_d}\|x\|^2$, where $\underline{\gamma_d} = \lambda_{\min}(P_d)$ and $\overline{\gamma_d} = \lambda_{\max}(P_d)$. Taking the time derivative of $V_d(x)$, using the definition of $x(t)$ in (1), substituting (24), (19), and simplifying yields

$$\dot{V}_d = -\tau \xi_{c^*}^T \Lambda \xi_{c^*} + \xi_{c^*}^T \Theta^T \Psi - \frac{\varepsilon_2}{2\tau^2} e_p^T \Gamma e_p - \frac{\varepsilon_2}{2\tau} e_p^T \Lambda \xi_{c^*} + \frac{\varepsilon_2}{2\tau^2} e_p^T \Theta^T \Psi + \frac{\varepsilon_2}{2} \xi_{c^*}^T \xi_{c^*}. \tag{28}$$

The DMP gain relations are selected as per [34] to be $\alpha_v = 4\beta_v$ and $\alpha_\omega = 4\beta_\omega$ to make a proportional–derivative-like part of the system critically damped. Defining the constants $\bar{c}_1 \ge (\varepsilon_2 \bar{\Theta}\overline{\Psi}/2\tau^2)$, $\bar{c}_2 \ge (2\tau^2 \bar{c}_1/\varepsilon_2)$, $C = \max\{\bar{c}_1, \bar{c}_2\}$, if β_v and β_w are chosen according to the sufficient conditions in (26), then (28) can be upper bounded as $\dot{V}_d \le -\lambda_d \|x\|^2 + \sqrt{2} C e^{-\underline{\alpha}(t-t_0)}\|x\|$, where $\lambda_d = \min\{(\varepsilon_2 \beta_v^2/\tau^2), 4\tau\beta_v - (3\varepsilon_2/2), (\varepsilon_2 \beta_\omega^2/\tau^2), 4\tau\beta_\omega - (3\varepsilon_2/2)\}$. Completing the squares and using the bounds on the Lyapunov function yields

$$\begin{aligned} \dot{V}_d &\le -\frac{\lambda_d}{2\bar{\gamma}_d} V_d + \frac{C^2}{\lambda_d} e^{-2\underline{\alpha}(t-t_0)} \\ &\le -\beta_2 V_d + \varpi e^{-2\underline{\alpha}(t-t_0)} \end{aligned} \tag{29}$$

where $\beta_2 = (\lambda_d/2\bar{\gamma}_d)$ and $\varpi = (C^2/\lambda_d)$. The solution to the differential inequality in (29) can be obtained using [29, Lemma 3.4] as

$$V_d(x(t)) \le V_d(x(t_0)) e^{-\beta_2(t-t_0)} + \bar{\varrho} e^{-\underline{c}_3(t-t_0)} \tag{30}$$

where $\underline{c}_3 = \min\{2\underline{\alpha}, \beta_2\}$, $\bar{\varrho} = (\varpi/|\beta_2 - 2\underline{\alpha}|)$, and $\beta_2 \ne 2\underline{\alpha}$ such that $|\cdot|$ denotes the absolute value of the argument. Using (30) and the bounds on the Lyapunov function, it can be concluded that $\|x(t)\| \in \mathcal{L}_\infty$. The second term on the right-hand side of (29) is a non-negative continuous perturbation term which satisfies $\lim_{t\to\infty} \varpi e^{-2\underline{\alpha}(t-t_0)} = 0$ resulting in the global asymptotic stability of the solution trajectories $x(t)$ (c.f. [29, Lemma 9.6]). ■

V. Stability Analysis of the Switched System

In this section, the stability of the switched system is analyzed while switching between DMP and IBVS controllers. To facilitate the stability analysis, the common state defined in (1) and stability results, which are derived for the dynamics of the common state using IBVS control and DMP, are used. The switched system switches between the IBVS controller in (6) and DMP in (19) based on the visibility of feature points. The switching between the controllers leads to discontinuous dynamics which can be mathematically expressed as

$$\dot{x} = f_{\sigma(x,t)}(x,t) + g_{\sigma(x,t)}(t), \quad \sigma : \mathbb{R}^{12} \times \mathbb{R}^+ \to \{v, d\}. \tag{31}$$

The switching signal $\sigma(x,t)$ governs the dynamics of $x(t)$. Since the IBVS exponentially converges to a bound when initialized in a local region near the goal state, a threshold constant $\delta_2 > 0$ is selected for the IBVS controller to be active such that, $x(t) \in \mathcal{B}_{\delta_2}(0) \subset \mathcal{B}_{\delta_1}(0)$. The relation between the positive constants δ_1 and δ_2 is established using the analysis in Theorem 3.

Remark 6: In practice, a threshold for image pixel error $e_i(t)$ and velocity $\xi_{c^*}(t)$, which corresponds to δ_2, can be chosen based on the image size and feature visibility. The IBVS system is active when all the features are detected, matched, and $\underline{\iota} \le e_i(t) \le \bar{\iota}$ for some suitably chosen vector $\bar{\iota} > \underline{\iota}$, where the inequalities are element-wise. No threshold is selected for the velocities $\xi_{c^*}(t)$, however, the constant τ in (19) can be adjusted to generate slow velocities using the DMP.

Let $\bar{\kappa} = \max\{\overline{\gamma_v}, \overline{\gamma_d}\}$, $\underline{\kappa} = \min\{\underline{\gamma_v}, \underline{\gamma_d}\}$, $\mu = (\bar{\kappa}/\underline{\kappa})$ be constants. The Lyapunov functions $V_v(x,t)$ and $V_d(x)$ in (13) and (27) can then be related as follows:

$$V_v \le \mu V_d, \quad V_d \le \mu V_v \quad \forall x(t) \in \mathcal{B}_{\delta_1}(0). \tag{32}$$

Definition 1 [10, Ch. 3, p. 58]: The switching signal $\sigma(x,t)$ has average dwell time τ_a, if there exist two numbers $N_0 \in \mathbb{Z}^+$ and $\tau_a \in \mathbb{R}^+$ such that

$$N_\sigma(t,\underline{t}) \leq N_0 + \frac{t-\underline{t}}{\tau_a} \tag{33}$$

is satisfied, where N_0 is known as the chatter bound and $N_\sigma(t,\underline{t})$ are the number of discontinuities on the interval $[\underline{t}, t)$.

Theorem 3: Provided that Assumptions 1–4 hold, the state trajectories of the switched system generated by the family of subsystems described by (31) and a piecewise constant, right continuous switching signal $\sigma : \mathbb{R}^{12} \times \mathbb{R}^+ \to \{v, d\}$ asymptotically converges to a bound in the sense that

$$\limsup_{t\to\infty} \|x(t)\| \leq \sqrt{\frac{\overline{\kappa}^{N_0+1}\eta}{\underline{\kappa}^{N_0+2}\epsilon}} \tag{34}$$

provided that:

I. If $x(t) \in \mathbb{R}^{12} \setminus \mathcal{B}_{\delta_1}(0) \Rightarrow \sigma(x,t) = d$.

II. If $\sigma(x(t^-), t^-) = 2$ and $x(t) \in \mathcal{B}_{\delta_2}(0)$, then $\sigma(x(t), t) = 1$.

III. The local region of convergence and the switching threshold satisfy the following conditions:

$$\sqrt{\frac{\underline{\kappa}^{N_0+2}}{\overline{\kappa}^{N_0+2}}}\delta_1 > \delta_2, \text{ and } \delta_1 > \sqrt{\frac{\overline{\kappa}^{N_0+1}\eta}{\underline{\kappa}^{N_0+2}\epsilon}}. \tag{35}$$

IV. The condition in (33) is satisfied for

$$\tau_a > \frac{\ln\mu}{\underline{\beta} - \epsilon} \tag{36}$$

where $0 < \epsilon < \underline{\beta} \leq \min\{(\beta_1/\overline{\gamma_v}), \underline{c_3}\}$.

Proof: The proof of the theorem is divided into two cases to characterize the behavior of the switched system in different regions of the space. Consider the Lyapunov function defined in (13) and (27)

$$V_{\sigma(x,t)}(x,t) = \begin{cases} x^T P_v(t) x + \tilde{\mathcal{O}} & \sigma(x,t) = v \\ x^T P_d x & \sigma(x,t) = d. \end{cases} \tag{37}$$

Case 1: When $\|x(t)\| > \delta_2$, the state $x(t) \in \mathbb{R}^{12} \setminus \mathcal{B}_{\delta_2}(0)$ is outside of the switching set for IBVS. If Condition I of Theorem 3 is satisfied, then $V_{\sigma(x,t)}(x,t)$ is differentiable and decreases exponentially from any initial condition. Then $\forall t \in [0, t_0)$ for $t_0 > 0$, the following upper bound holds:

$$\begin{aligned} V_\sigma(x(t),t) &\leq V_\sigma(x(0),0)e^{-\underline{\beta}_2 t} + \bar{\varrho}e^{-\underline{c}_3 t} \\ &\leq (V_\sigma(x(0),0) + \bar{\varrho})e^{-\underline{\beta} t} \end{aligned} \tag{38}$$

where $\sigma : \mathbb{R}^{12} \setminus \mathcal{B}_{\delta_2}(0) \times [0, t_0) \to d$ and the arguments of σ are dropped in (38) for brevity. The time required to reach the set $\mathcal{B}_{\delta_2}(0)$ from any initial condition is finite and can be lower bounded by $t_0 \geq (1/\underline{\beta})\ln(\min\{([\overline{\gamma_d}\|x(t_0)\|^2 + \bar{\varrho}]/\underline{\gamma_d}\delta_2^2), 1\})$. The controller switches to IBVS when $\|x(t_0)\| < \delta_2$. The switched system state trajectories after switching to and operating in IBVS thereafter remain in a subset of the local region, i.e., $\|x(t_0)\| < \delta_2 \Rightarrow \|x(t)\| < \delta_1$, if $\sigma(x,t) = v \;\forall\; t \geq t_0$, and condition III is satisfied.

Case 2: Let $t_0 = \inf\{t \in \mathbb{R}^+ | \|x(t)\| < \delta_2\} \geq 0$ be the first time instance when $\|x(t)\| < \delta_2$ implying that $x(t_0) \in \mathcal{B}_{\delta_2}(0)$. Such a $t_0 < \infty$ exists due to exponentially decaying upper bound in (38). Using a recursion similar to the results in [35], Lyapunov bounds in (18) and (30), and the average dwell-time condition in (33) and (36), the conservative bound on the solution of the Lyapunov function in (37) between the interval $[t_0, t)$ for monotonically increasing sequence of switching times $\{t_n\}_{n=0}^{N_\sigma(t_0,t)}$ can be given as

$$\begin{aligned} V_\sigma(x(t),t) \leq \mu^{N_0+1}\Big((V_\sigma(x(t_0),t_0) + \bar{w})e^{-\epsilon(t-t_0)} \\ + \frac{\eta}{\epsilon}\Big(1 - e^{-\epsilon(t-t_0)}\Big)\Big) \quad \forall x(t) \in \mathcal{B}_{\delta_1}(0) \end{aligned} \tag{39}$$

where $\bar{w} = \varpi/(2\underline{\alpha} - \epsilon)$. For large enough t, the solution $x(t)$ never exits the region $\mathcal{B}_{\delta_1}(0)$. It can be concluded from (39) that $x(t)$ is continuous, $x(t) \in \mathcal{L}_\infty$ and converges asymptotically to the bound in (34). ■

The ultimate bound on the switched system is larger compared to the bound on the individual IBVS system as switching between subsystems can lead to the growth of the Lyapunov function. Such a bound is commonly found in the literature in different contexts (c.f. [36, Th. 1], [27, Lemma 2], and [37, Th. 1]). Algorithm 1 is developed based on the stability analysis presented in Theorem 3 to ensure stable switching by compensating for the fast switching occurring due to the disturbances and occlusions in the IBVS subsystem. A compensation time t_c is calculated and the DMP subsystem is kept active for additional time to ensure that the average dwell-time condition is satisfied for a total of $\bar{N} > 0$ switches.

Remark 7: Theorem 3 establishes the general conditions for switching between the subsystems and is useful in the case of frequent perturbations or occlusions which can result in fast switching which can make the combined system unstable if the average dwell-time condition is not satisfied.

Remark 8: The constant $\underline{\beta}$ depends on the IBVS controller gains k_p and k_v and the DMP gains α_v, α_ω, β_v, β_ω, α_{z_p}, and α_{z_o}. Increasing the gains can increase $\underline{\beta}$ which enables the user to choose ϵ from a wider range of values. Choosing a high value of ϵ leads to a faster convergence of the bound in (39). However, this increases the average dwell time τ_a in (36). On the other hand, if ϵ is chosen to be small, the bound in (39) converges slowly but allows for a lower τ_a.

VI. Experiments

A. Experimental Setup

The camera in the wrist of the right arm of a Baxter research robot is used to capture images of an ArUco marker with the frame rate of 30 frames/s and image resolution 640×420. The corners of the ArUco marker are used as feature points ($m = 4$) for IBVS. The feature points are detected and matched using OpenCV's ArUco library. The processing is done at 30frames/s using a desktop with an Intel Core2Duo CPU with a clock speed of 2.26 GHz and 4-GB RAM running Ubuntu 14.04. The experimental setup is shown in Fig. 3. The DMP-IBVS switching algorithm is implemented in MATLAB 2018a. The camera intrinsic parameters for Baxter's right hand camera are given by $f_x = f_y = 407.1$, $c_x = 323.4$, and $c_y = 205.6$, where f_x, f_y represent the camera focal lengths in pixels and (c_x, c_y) represents the camera center pixel.

Algorithm 1: Algorithm for Switching Between IBVS and DMP Based on Visibility of Feature Points and Average Dwell-Time Condition

Select decay rates $\underline{\beta}, \epsilon > 0$, chatter bound $N_0 \geq 1$, feature error thresholds $\bar{\iota} > \underline{\iota}$;
Compute $\mu = \frac{\bar{\kappa}}{\underline{\kappa}}$ and $\tau_a = \frac{\ln \mu}{\underline{\beta} - \epsilon}$;
Set $t_d = 0$ and $t_v = 0$ to be the last time instant when DMP and IBVS were active respectively;
Set $t_e = 0$ as the elapsed time and $\bar{N} > 1$ as the number of switches over which the dwell time condition should be satisfied;
Set the compensation time $t_c = 0$ and current number of switches $N_\sigma = 0$;
while *data is available* **do**
  if *features match* & $\underline{\iota} \leq e_i \leq \bar{\iota}$ & $t > t_v + t_c$ **then**
    Run IBVS according to (6);
    if $t_d > t_v$ **then**
      $t_e \leftarrow t_e + (t_d - t_v)$;
      $N_\sigma \leftarrow N_\sigma + 1$;
      $t_c \leftarrow 0$;
    $t_v \leftarrow t$;
  else
    Run DMP according to (19);
    if $t_v > t_d$ **then**
      $N_\sigma \leftarrow N_\sigma + 1$;
      $t_e \leftarrow t_e + (t_v - t_d)$;
      if $N_\sigma \geq \bar{N}$ **then**
        $t_c \leftarrow (N_\sigma - N_0)\tau_a - t_e$;
        $t_e \leftarrow 0$;
        $N_\sigma \leftarrow 0$;
    $t_d \leftarrow t$;
end

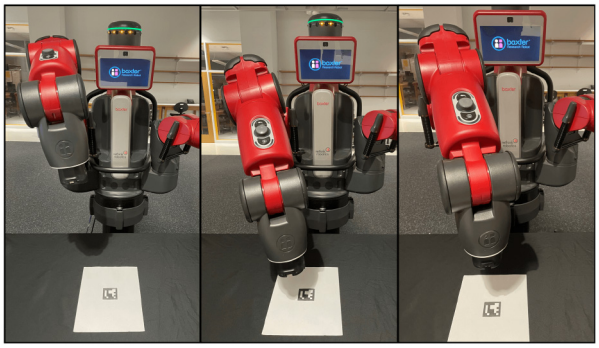

Fig. 3. Experimental setup showing Baxter's end effector with an eye-in-hand configuration observing the ArUco marker.

The position DMP is trained on a demonstration trajectory, which is collected by recording Baxter's arm position, velocity, acceleration, and filtered using a constant acceleration Kalman filter. The orientation DMP is trained on a trajectory generated by a minimum-jerk polynomial for quaternions. The goal pose of the DMP is used to record the desired feature vector s_i^* for the IBVS system. The DMP acceleration commands are computed from the Baxter robot pose feedback. The IBVS and DMP controller-generated acceleration is integrated and applied as a joint velocity controller using the pseudoinverse of the Baxter manipulator Jacobian matrix.

B. Experiment 1

In this experiment, the convergence and stability of the DMP-IBVS switched system is verified when switching occurs only once. The DMP weights are computed by recording a trajectory as described earlier. The DMP parameters are set to $\alpha_v = 140$, $\beta_v = 35$, $\alpha_\omega = 4$, $\beta_\omega = 1$, $\alpha_{z_p} = 1$, $\alpha_{z_o} = 1$, and $\tau = 25$. The IBVS gains are empirically tuned to be $k_p = 5$, and $k_v = 10$. The initial pose of the Baxter right-hand camera is selected such that none of the desired feature points are in the FOV of the camera. The feature threshold error for switching is chosen as $\bar{\iota} = [0.85, 0.42, \cdots, 0.85, 0.42]^T$, $\underline{\iota} = -\bar{\iota}$ which corresponds to pixel errors of 345 and 170 pixels in the X- and Y-directions of the image frame, respectively. When the features are out of the FOV, the arm starts approaching the goal location along the trained DMP trajectory. The controller switches to IBVS once the features are in the FOV of the camera and the feature error is less than the selected threshold error, i.e., $\underline{\iota} \leq e_i \leq \bar{\iota}$. This condition is first satisfied at $t = 16.4$ s. Fig. 4(a) shows the acceleration generated by the switched system with the discontinuity at 16.4 s, which is the switching instance. The pose error starts converging to the desired pose as the DMP is active until $t = 16.4$ s. Once the switch to IBVS happens, the pose error in Fig. 4(b) converges to a bound. It is also observed that the pose error is continuous as proven in Theorem 3. Fig. 4(c) shows the image feature error $e_i(t)$, which is first computed when all the features are visible and the threshold condition is satisfied. The image feature error decreases exponentially to a bound as the IBVS system converges. Fig. 4(d) shows the Lyapunov function $V_{\sigma(x,t)}(x(t), t)$ for the switched system. The orange line shows $V_v(x(t), t)$ and the right y-axis represents its values. Similarly, the blue line shows $V_d(x(t))$ and the left y-axis represents its values. The Lyapunov functions are only plotted for the active subsystem in the corresponding time interval. The Lyapunov function asymptotically decreases for both controllers when active individually, verifying the result of Theorem 3. The error bounds obtained for the experiment in Table I verify the convergence of the error for the switched system. The error bounds are computed by taking the average of the last five error data points.

C. Experiment 2

In the second experiment, the stability and convergence of the DMP-IBVS switched system are tested when there are multiple switches amongst these individual systems. Such a case would occur practically when the feature points are occluded or the features go out of FOV during the IBVS system operation. The feature occlusion is simulated using a piece of paper placed on the ArUco markers covering the camera view. The parameters of the DMP-IBVS switching algorithm are selected empirically as follows: $\mu = 10.67$,

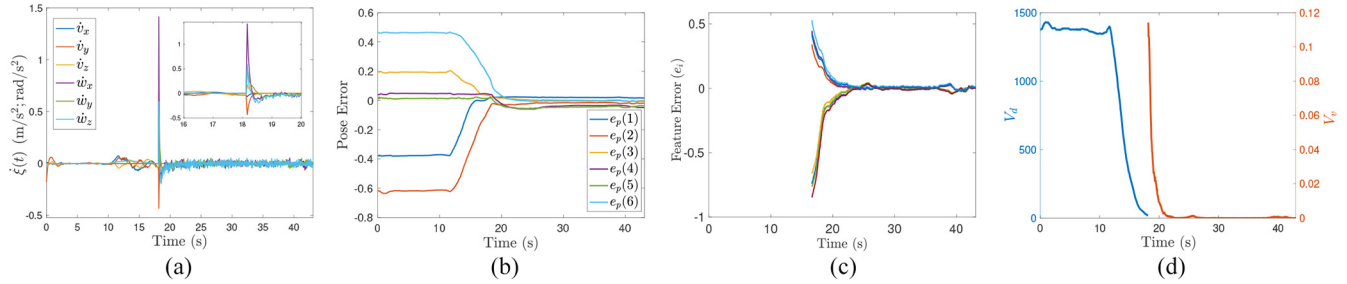

Fig. 4. Experimental results for the DMP and IBVS for a single switching instance at 16.4 s. (a) Camera acceleration generated by the DMP controller till 16.4 s and camera acceleration generated by the IBVS controller after 16.4 s. (b) Pose error $e_p(t)$ converges to a bound. (c) Image feature errors $e_i(t)$ computed after 16.4 s. (d) Value of Lyapunov function $V_{\sigma(x,t)}(x(t),t)$, with the left y-axis showing the scale for $V_d(x(t))$ and the right y-axis showing the scale for $V_v(x(t),t)$.

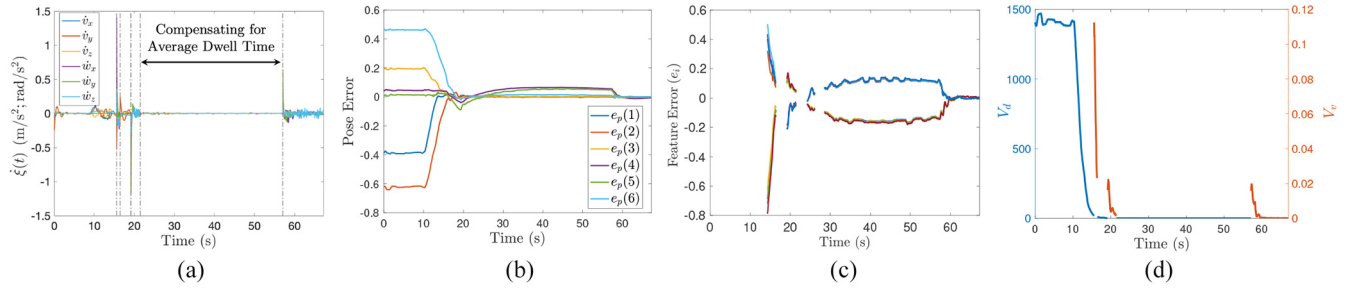

Fig. 5. Experimental results for the DMP and IBVS with frequent feature occlusion. (a) Camera acceleration generated by the DMP controller and the IBVS controller in the presence of occlusion with gray dashed-dotted lines showing the switching instances. (b) Pose error $e_p(t)$ converges to a bound in the presence of multiple switching instances. (c) Image feature errors $e_i(t)$ computed when all the features are visible and satisfy the threshold condition in Algorithm 1. (d) Value of Lyapunov function $V_{\sigma(x,t)}(x(t),t)$ during multiple switching instances, with the left y-axis showing the scale for $V_d(x(t))$ and the right y-axis showing the scale for $V_v(x(t),t)$.

the decay rates are $\underline{\beta} = 0.77$ and $\epsilon = 0.01\underline{\beta}$. The average dwell time is calculated as $\tau_a = 13.82$ s. The individual DMP and IBVS parameters are the same as those from Experiment 1. The constants are selected as $\bar{N} = 5$ and $N_0 = 2$, which allows the total time between $\bar{N}$ switches to be $3\tau_a$. This also implies that if the first four switches between IBVS and DMP controllers are fast, then the DMP-IBVS system ensures that the average dwell-time condition is met by keeping the DMP controller active for longer time before the 5th switch occurs. The results of Experiment 2 are summarized in Fig. 5(a)–(d). Fig. 5(a) shows the acceleration generated by the switched system with the switching instants marked with gray dashed-dotted lines. The switching occurs at the following time instances $t = 15.56$ s, $t = 16.44$ s, $t = 19.12$ s, $t = 21.48$ s, and $t = 57.08$ s with the DMP controller active between 0 and 15.56 s. Fig. 5(b) shows the convergence of the pose error to a bound for the switched system using Algorithm 1. As verified by Theorem 3, the pose error is continuous despite the switching between the DMP and IBVS subsystems. Fig. 5(c) shows the exponential decay of the image feature errors when the IBVS controller is active and the conditions of Algorithm 1 are met. It can be seen that, although all the features are visible and the feature error is below the selected threshold, the DMP controller is active between $t = 21.48$–57.08 s to compensate for the average dwell time to ensure the stability despite fast initial switching. Fig. 5(d) shows the asymptotic convergence of the Lyapunov function $V_{\sigma(x,t)}(x(t),t)$ for the switched system. The result of Theorem 3 is verified by the stability of the Lyapunov functions as shown in Fig. 5(d). The error bounds obtained for the experiment in Table I verify the convergence of the error for the switched system.

TABLE I
ERROR BOUND INFORMATION FOR BAXTER POSE REGULATION EXPERIMENTS

	$\|x\|$	$\|\rho\|$	$\|e_i\|$	$\|e_p\|$
Experiment 1	0.0660	0.0240	0.0239	0.0658
Experiment 2	0.0089	0.0078	0.0078	0.0082

D. Experiment 3

In this experiment, the DMP-IBVS switched system performance is compared with the performance of DMP for a precision pose regulation task of the end effector when there is an uncertainty in the goal pose. Precision positioning is required in many fine manipulation tasks, such as assembly, small hole insertions, or pinch grasping. A pinch grasp task using parallel jaw grippers is considered in this experiment. For successful pinch grasping the gripper needs to be positioned precisely to a certain pose (i.e., a goal pose) with respect to the object. An ArUco marker is attached to an object which is placed in a box for this task. The DMP-only control and the DMP-IBVS control are implemented. Trajectory data starting from a pose where the object is not visible in the camera FOV due to the presence of the box and ending close to the object before the gripper closes for pinching is collected for training the DMP parameters. The object position in the box

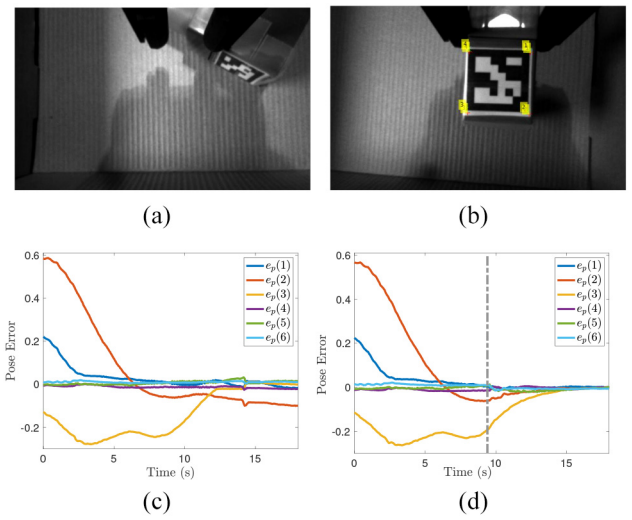

Fig. 6. Experimental results for end-effector positioning to complete the pinch grasping task with changed object location. (a) Failed pinching operation with changed object location using the DMP-only system. (b) Successful pinching operation despite changed goal location using the DMP-IBVS switched system. (c) Pose error evolution for the DMP. (d) Pose error convergence for the DMP-IBVS switched system.

is slightly changed during testing before the trajectory is generated using the DMP-only and DMP-IBVS switched system. The changed goal pose due to the change of object location is unknown to the DMP. Thus, the DMP-only system cannot reach the new pose. In Fig. 6(a), the pinch grasp operation fails using the DMP-only system because the gripper could not position itself precisely before the parallel jaw gripper is activated. However, the DMP-IBVS switched system is able to adapt to the change in the goal pose of the gripper using eye-in-hand image feedback once it is available. The successful pinch using the DMP-IBVS switched system is shown in Fig. 6(b). Fig. 6(c) and (d) shows the evolution of the pose error e_p computed with respect to the new goal pose for the DMP-only and DMP-IBVS switched system. As seen by the dashed-dotted gray line in Fig. 6(d), the DMP is active until 9.40 s and then the IBVS subsystem becomes active when image features are visible. The IBVS ensures the convergence of the pose error with respect to the object using image feedback. The DMP-only system on the other hand is not able to adapt to the change in goal pose and converges to the goal pose used during training. As a result, the pose error does not converge to zero as seen from Fig. 6(c). The pose error computed in terms of $\|e_p\|$ for the DMP system is 0.1105 whereas for the DMP-IBVS switched system is 0.0092.

VII. Conclusion

In this article a switching strategy is presented, that utilizes DMP and IBVS methodologies to combine learning-based end-effector control and perception-based control. The Lyapunov stability analysis of the proposed IBVS system yields a UUB result in a local region around the origin, and that of the DMP system yields global asymptotic stability. The switched DMP-IBVS system analysis based on multiple Lyapunov functions shows that the switched system asymptotically converges to a bound. A switching algorithm is presented based on feature visibility while maintaining stability subject to the average dwell-time condition. The method is tested on a Baxter research robot using a pose regulation task of the robot's end effector over an ArUco marker placed on a table. Future work will involve analysis of multiple equilibria when the object is moved and applying the developed method in various manufacturing and space robotics applications.

References

[1] E. Tunstel et al., "Robotic wire pinning for wire harness assembly automation," in *Proc. IEEE/ASME Int. Conf. Adv. Intell. Mechatronics (AIM)*, 2020, pp. 1208–1215.
[2] A. J. Ijspeert, J. Nakanishi, and S. Schaal, "Learning attractor landscapes for learning motor primitives," in *Proc. Int. Conf. Adv. Neural Inf. Process. Syst.*, 2003, pp. 1547–1554.
[3] F. Chaumette and S. Hutchinson, "Visual servo control. I. Basic approaches," *IEEE Robot. Autom. Mag.*, vol. 13, no. 4, pp. 82–90, Dec. 2006.
[4] G. López-Nicolás, N. R. Gans, S. Bhattacharya, C. Sagüés, J. J. Guerrero, and S. Hutchinson, "Homography-based control scheme for mobile robots with nonholonomic and field-of-view constraints," *IEEE Trans. Syst., Man, Cybern. B, Cybern.*, vol. 40, no. 4, pp. 1115–1127, Aug. 2010.
[5] N. R. Gans, G. Hu, K. Nagarajan, and W. E. Dixon, "Keeping multiple moving targets in the field of view of a mobile camera," *IEEE Trans. Robot.*, vol. 27, no. 4, pp. 822–828, Aug. 2011.
[6] I. Salehi, G. Rotithor, R. Saltus, and A. P. Dani, "Constrained image-based visual servoing using barrier functions," in *Proc. IEEE Int. Conf. Robot. Autom.*, 2021, pp. 14254–14260.
[7] R. Wang, X. Zhang, Y. Fang, and B. Li, "Virtual-goal-guided RRT for visual servoing of mobile robots with FOV constraint," *IEEE Trans. Syst., Man, Cybern., Syst.*, vol. 52, no. 4, pp. 2073–2083, Apr. 2022.
[8] Y. Huang, M. Zhu, Z. Zheng, and K. H. Low, "Linear velocity-free visual servoing control for unmanned helicopter landing on a ship with visibility constraint," *IEEE Trans. Syst., Man, Cybern., Syst.*, vol. 52, no. 5, pp. 2979–2993, May 2022.
[9] F. Ke, Z. Li, H. Xiao, and X. Zhang, "Visual servoing of constrained mobile robots based on model predictive control," *IEEE Trans. Syst., Man, Cybern., Syst.*, vol. 47, no. 7, pp. 1428–1438, Jul. 2017.
[10] D. Liberzon, *Switching in Systems and Control*. Boston, MA, USA: Birkhauser, 2003.
[11] D. Liberzon and A. S. Morse, "Basic problems in stability and design of switched systems," *IEEE Control Syst. Mag.*, vol. 19, no. 5, pp. 59–70, Oct. 1999.
[12] J. P. Hespanha and A. S. Morse, "Stability of switched systems with average dwell-time," in *Proc. 38th IEEE Conf. Decis. Control*, vol. 3, 1999, pp. 2655–2660.
[13] J. Daafouz, P. Riedinger, and C. Iung, "Stability analysis and control synthesis for switched systems: A switched Lyapunov function approach," *IEEE Trans. Autom. Control*, vol. 47, no. 11, pp. 1883–1887, Nov. 2002.
[14] J. P. Hespanha, "Uniform stability of switched linear systems: Extensions of LaSalle's invariance principle," *IEEE Trans. Autom. Control*, vol. 49, no. 4, pp. 470–482, Apr. 2004.
[15] H. Lin and P. J. Antsaklis, "Stability and stabilizability of switched linear systems: A survey of recent results," *IEEE Trans. Autom. Control*, vol. 54, no. 2, pp. 308–322, Feb. 2009.
[16] M. S. Branicky, "Multiple Lyapunov functions and other analysis tools for switched and hybrid systems," *IEEE Trans. Autom. Control*, vol. 43, no. 4, pp. 475–482, Apr. 1998.
[17] R. Kamalapurkar, J. A. Rosenfeld, A. Parikh, A. R. Teel, and W. E. Dixon, "Invariance-like results for nonautonomous switched systems," *IEEE Trans. Autom. Control*, vol. 64, no. 2, pp. 614–627, Feb. 2019.
[18] D. Astolfi, R. Postoyan, and D. Nešić, "Uniting observers," *IEEE Trans. Autom. Control*, vol. 65, no. 7, pp. 2867–2882, Jul. 2020.
[19] C. Prieur and A. R. Teel, "Uniting local and global output feedback controllers," *IEEE Trans. Autom. Control*, vol. 56, no. 7, pp. 1636–1649, Jul. 2011.
[20] N. R. Gans and S. A. Hutchinson, "Stable visual servoing through hybrid switched-system control," *IEEE Trans. Robot.*, vol. 23, no. 3, pp. 530–540, Jun. 2007.

[21] A. Parikh, T.-H. Cheng, H.-Y. Chen, and W. E. Dixon, "A switched systems framework for guaranteed convergence of image-based observers with intermittent measurements," *IEEE Trans. Robot.*, vol. 33, no. 2, pp. 266–280, Apr. 2017.
[22] A. Parikh, R. Kamalapurkar, and W. E. Dixon, "Target tracking in the presence of intermittent measurements via motion model learning," *IEEE Trans. Robot.*, vol. 34, no. 3, pp. 805–819, Jun. 2018.
[23] A. Parikh, T.-H. Cheng, R. Licitra, and W. E. Dixon, "A switched systems approach to image-based localization of targets that temporarily leave the camera field of view," *IEEE Trans. Control Syst. Technol.*, vol. 26, no. 6, pp. 2149–2156, Nov. 2018.
[24] H. Chen, Z. I. Bell, P. Deptula, and W. E. Dixon, "A switched systems approach to path following with intermittent state feedback," *IEEE Trans. Robot.*, vol. 35, no. 3, pp. 725–733, Jun. 2019.
[25] C. G. Harris, Z. I. Bell, E. A. Doucette, J. W. Curtis, and W. E. Dixon, "Target tracking in the presence of intermittent measurements by a sparsely distributed network of stationary cameras," in *Proc. Amer. Control Conf.*, 2020, pp. 3491–3496.
[26] H.-Y. Chen, Z. I. Bell, P. Deptula, and W. E. Dixon, "A switched systems framework for path following with intermittent state feedback," *IEEE Control Syst. Lett.*, vol. 2, pp. 749–754, 2018.
[27] S. Veer and I. Poulakakis, "Switched systems with multiple equilibria under disturbances: Boundedness and practical stability," *IEEE Trans. Autom. Control*, vol. 65, no. 6, pp. 2371–2386, Jun. 2020.
[28] G. Rotithor and A. P. Dani, "Combining motion primitives and image-based visual servo control," in *Proc. Int. Symp. Flexible Autom.*, 2020, p. 5.
[29] H. K. Khalil, *Nonlinear Systems*, 3rd ed. Upper Saddle River, NJ, USA: Prentice-Hall, 2002.
[30] G. Rotithor, D. Trombetta, R. Kamalapurkar, and A. P. Dani, "Full- and reduced-order observers for image-based depth estimation using concurrent learning," *IEEE Trans. Control Syst. Technol.*, vol. 29, no. 6, pp. 2647–2653, Nov. 2021.
[31] M. W. Spong, S. Hutchinson, and M. Vidyasagar, *Robot Modeling and Control*, vol. 3. New York, NY, USA: Wiley, 2006.
[32] F. Chaumette, "Potential problems of stability and convergence in image-based and position-based visual servoing," in *The Confluence of Vision and Control*. London, U.K.: Springer-Verlag, 1998, pp. 66–78.
[33] D. Han, Q. Wei, Z. Li, and W. Sun, "Control of oriented mechanical systems: A method based on dual quaternion," *IFAC Proc. Vol.*, vol. 41, no. 2, pp. 3836–3841, 2008.
[34] A. Ude, B. Nemec, T. Petrić, and J. Morimoto, "Orientation in cartesian space dynamic movement primitives," in *Proc. IEEE Int. Conf. Robot. Autom. (ICRA)*, 2014, pp. 2997–3004.
[35] L. Vu, D. Chatterjee, and D. Liberzon, "Input-to-state stability of switched systems and switching adaptive control," *Automatica*, vol. 43, no. 4, pp. 639–646, 2007.
[36] J. R. Klotz, A. Parikh, T.-H. Cheng, and W. E. Dixon, "Decentralized synchronization of uncertain nonlinear systems with a reputation algorithm," *IEEE Trans. Control Netw. Syst.*, vol. 5, no. 1, pp. 434–445, Mar. 2018.
[37] J. Ye, S. Roy, M. Godjevac, and S. Baldi, "A switching control perspective on the offshore construction scenario of heavy-lift vessels," *IEEE Trans. Control Syst. Technol.*, vol. 29, no. 1, pp. 470–477, Jan. 2021.

Ghananeel Rotithor (Graduate Student Member, IEEE) received the M.S. degree in biomedical engineering from the University of Florida, Gainesville, FL, USA, in 2017. He is currently pursuing the Ph.D. degree with the Electrical and Computer Engineering Department, University of Connecticut, Storrs, CT, USA.

His research interests include robot perception, and state estimation and control.

Mr. Rotithor is a co-recipient of the 2020 IFAC Applications Paper Award Finalist.

Iman Salehi (Member, IEEE) received the master's degree from the Department of Electrical and Computer Engineering, University of Hartford, West Hartford, CT, USA, in 2015. He is currently pursuing the Ph.D. degree with the Electrical and Computer Engineering Department, University of Connecticut, Storrs, CT, USA.

His research interests include learning for control, human–robot interaction, and system identification.

Mr. Salehi is a co-recipient of the 2020 IFAC Applications Paper Award Finalist and the recipient of the 2020 IEEE L-CSS Outstanding Reviewer Award.

Edward Tunstel (Fellow, IEEE) received the B.S. and M.E. degrees in mechanical engineering from Howard University, Washington, DC, USA, in 1986 and 1989, respectively, and the Ph.D. degree in electrical engineering from the University of New Mexico, Albuquerque, NM, USA, in 1996.

He served as a Leader of Robotics and Autonomy with NASA Jet Propulsion Laboratory, Pasadena, CA, USA, from 1989 to 2007, Johns Hopkins Applied Physics Laboratory, Laurel, MD, USA, from 2007 to 2017, and Raytheon Technologies Research Center, East Hartford, CT, USA, from 2017 to 2021. He was an Associate Director and the Group Leader of Robotics with the Autonomous and Intelligent Systems Department, Raytheon Technologies Research Center, focused on research and development and transition of technologies enabling autonomy and human-collaborative capabilities for service and manufacturing applications. He is currently the CTO of Motiv Space Systems, Inc., Pasadena. He has authored more than 170 technical publications, including five coauthored and co-edited books spanning areas of robotics and autonomous systems.

Dr. Tunstel is a member of the IEEE Robotics and Automation Society and a Senior Member of AIAA, and was the 2018–2019 President of the IEEE Systems, Man, and Cybernetics Society.

Ashwin P. Dani (Senior Member, IEEE) received the M.S. and Ph.D. degrees in mechanical and aerospace engineering from the University of Florida (UF), Gainesville, FL, USA, in 2008 and 2011, respectively.

He is currently an Associate Professor with the Department of Electrical and Computer Engineering, University of Connecticut, Storrs, CT, USA. He was a Postdoctoral Research Associate with the University of Illinois at Urbana–Champaign, Champaign, IL, USA. His research interests are in the areas of estimation and control, learning for control, vision-based estimation and control, and human–robot collaboration.

Dr. Dani is a co-recipient of the 2020 IFAC Applications Paper Award Finalist, the 2016 FUSION Student Paper Award—1st Runner Up, the 2015 ASME Dynamics, Systems and Controls Conference Robotics Paper Award, and the 2012 Technology Innovator Award from UF. He is an Associate Editor of IEEE TRANSACTIONS ON MECHATRONICS and a member of the Conference Editorial Board for IEEE Control System Society.